

## COMMUNICATION

[View Article Online](#)  
[View Journal](#) | [View Issue](#)Cite this: *J. Mater. Chem. A*, 2020, **8**, 7117Received 12th February 2020  
Accepted 24th March 2020

DOI: 10.1039/d0ta01688h

[rsc.li/materials-a](http://rsc.li/materials-a)**Mo-doped SnS<sub>2</sub> with enriched S-vacancies for highly efficient electrocatalytic N<sub>2</sub> reduction: the critical role of the Mo–Sn–Sn trimer†**

Ke Chu, \* Jing Wang, Ya-ping Liu, Qing-qing Li and Ya-li Guo

Vacancy engineering and heteroatom doping are two effective approaches to tailor the electronic structures of catalysts for improved electrocatalytic activity. Herein, these two approaches were rationally combined to modulate the structure of SnS<sub>2</sub> toward the N<sub>2</sub> reduction reaction (NRR) by means of Mo-doping, which simultaneously induced the generation of enriched S-vacancies (V<sub>s</sub>). The developed Mo-doped SnS<sub>2</sub> nanosheets with enriched V<sub>s</sub> presented a conspicuously enhanced NRR activity with an NH<sub>3</sub> yield of 41.3 μg h<sup>−1</sup> mg<sup>−1</sup> (−0.5 V) and a faradaic efficiency of 20.8% (−0.4 V) and are among the best SnS<sub>2</sub>-based NRR catalysts to date. Mechanistic studies revealed that the co-presence of the Mo dopant and V<sub>s</sub> enabled the creation of Mo–Sn–Sn trimer catalytic sites, capable of strongly activating N<sub>2</sub> even for the cleavage of the N≡N triple bond to the N=N double bond at the N<sub>2</sub> adsorption stage, consequently leading to a downhill process of the first hydrogenation step and a largely reduced energy barrier.

Dinitrogen (N<sub>2</sub>) fixation to ammonia (NH<sub>3</sub>) is an essential chemical process for the modern industrial society because NH<sub>3</sub> is a widely used feedstock for various chemical products and is also a promising carbon-free energy carrier.<sup>1</sup> The electrochemical N<sub>2</sub> reduction reaction (NRR) under ambient conditions holds great promise for green and sustainable NH<sub>3</sub> production,<sup>2</sup> in stark contrast to the industrial Haber–Bosch process which involves huge energy consumption and enormous CO<sub>2</sub> emission. However, the NRR process is largely limited by the unsatisfactory NH<sub>3</sub> production rate and low faradaic efficiency (FE), stemming from the extremely stable N≡N bond, poor N<sub>2</sub> adsorption/activation on the catalyst surface and the competing hydrogen evolution reaction (HER).<sup>3</sup> Exploring highly active electrocatalysts may hold the key to mitigating these limitations and realizing high NRR efficiency. Over the past three years, an increasingly large number of noble metals,<sup>4–7</sup> transition metal-based compounds,<sup>8–14</sup> and metal-free

materials<sup>15–19</sup> have been designed as promising candidates toward the NRR.

SnS<sub>2</sub>-based materials have shown great potential in electrolysis applications, owing to their fascinating catalytic performance, good stability, tunable electronic structures, and 2D morphology with largely exposed active edges.<sup>20</sup> Recently, SnS<sub>2</sub> has been proved to be an attractive catalyst with favorable NRR activity as well.<sup>21,22</sup> Nonetheless, the reported NRR performance of SnS<sub>2</sub> materials is still far from satisfactory and competitive with that of the state-of-the-art NRR catalysts. The main bottlenecks are the poor NRR activation, *i.e.*, the high energy barrier for the first hydrogenation step,<sup>22</sup> and the low intrinsic electrical conductivity, *i.e.*, the inefficient proton-coupled electron transfer process, even when employing approaches such as growth of amorphous Sn on crystalline SnS<sub>2</sub> nanosheets (FE: 6.5%)<sup>21</sup> and construction of well-aligned SnS<sub>2</sub> nanoarrays on porous Ni foam (FE: 11.2%).<sup>22</sup> Thus, more efficient methods are still needed to further enhance the intrinsic NRR activity of SnS<sub>2</sub>.

As an effective strategy for electronic structure modulation of the catalysts, vacancy engineering by introducing anion vacancies into the catalyst lattice,<sup>23</sup> such as oxygen vacancies (TiO<sub>2</sub>,<sup>24</sup> WO<sub>3</sub> (ref. 25) and MnO<sub>2</sub> (ref. 26)), and nitrogen vacancies (C<sub>3</sub>N<sub>4</sub>,<sup>27</sup> VN<sup>28</sup> and W<sub>2</sub>N<sub>3</sub> (ref. 29)), provides unique active sites for the effective adsorption and activation of dinitrogen. In addition, heteroatom doping is another widely used method to optimize the adsorption of NRR intermediates on catalysts and promote the NRR reaction kinetics,<sup>30–33</sup> which have been demonstrated in V-doped TiO<sub>2</sub>,<sup>34</sup> Fe-doped Ni<sub>2</sub>P<sup>35</sup> and Mo-doped MnO<sub>2</sub>.<sup>36</sup> More importantly, heteroatom doping has been recently confirmed to facilitate the generation of vacancies, while the synergistic effect of dopants and vacancies leads to a conspicuously enhanced NRR performance.<sup>37,38</sup> For instance, introducing Zr-dopants in TiO<sub>2</sub> nanotubes has been reported to favorably generate both enriched oxygen vacancies and bi-Ti<sup>3+</sup> pairs,<sup>38</sup> and the bi-Ti<sup>3+</sup> pairs serve as the dominant active sites in facilitating the catalytic performance of the NRR with an FE of 17.3%. Similar results and a more improved NRR

School of Materials Science and Engineering, Lanzhou Jiaotong University, Lanzhou 730070, China. E-mail: [chukelut@163.com](mailto:chukelut@163.com)

† Electronic supplementary information (ESI) available. See DOI: 10.1039/d0ta01688h

performance (FE: 25.6%) have been presented in Fe-doped  $\text{TiO}_2$  nanoparticles,<sup>37</sup> where the combined effect of bi- $\text{Ti}^{3+}$  pairs and oxygen vacancies contributes to the substantially boosted NRR activity. Inspired by these studies, it is anticipated that the NRR performance of  $\text{SnS}_2$  may be greatly enhanced by the combination of vacancy engineering and heteroatom doping.

In this study, we rationally combined vacancy engineering and heteroatom doping to regulate the electronic structure of  $\text{SnS}_2$  by Mo-doping, which enabled the spontaneous generation of enriched S-vacancies ( $V_s$ ) as well. The developed Mo-doped  $\text{SnS}_2$  nanosheets with enriched  $V_s$  exhibited a significantly enhanced NRR activity with an  $\text{NH}_3$  yield of  $41.3 \mu\text{g h}^{-1} \text{mg}^{-1}$  ( $-0.5 \text{ V}$ ) and an FE of 20.8% ( $-0.4 \text{ V}$ ) and were among the best  $\text{SnS}_2$ -based NRR catalysts to date. Density functional theory (DFT) calculations revealed that the co-presence of the Mo dopant and  $V_s$  enabled the creation of Mo-Sn-Sn trimer active sites that could strongly activate  $\text{N}_2$  and lower the reaction energy barrier.

Mo-doped  $\text{SnS}_2$  (Mo-SnS<sub>2</sub>) nanosheets were directly grown on CC *via* a facile hydrothermal method. Pristine  $\text{SnS}_2/\text{CC}$  was also prepared as a reference. The synthesis details are provided in the ESI.† The obtained  $\text{SnS}_2$  and Mo-SnS<sub>2</sub> nanosheets scraped from CC were first investigated by X-ray photoelectron spectroscopy (XPS). As shown in Fig. 1a, the deconvolution of the Mo3d spectrum results in three well-resolved peaks of S2s (226.4 eV),  $\text{Mo}^{4+}3d_{3/2}$  (229.3 eV) and  $\text{Mo}^{4+}3d_{1/2}$  (232.7 eV) for Mo-SnS<sub>2</sub> nanosheets, which are absent in pristine  $\text{SnS}_2$  nanosheets, indicating the successful Mo-doping in the Mo-SnS<sub>2</sub> nanosheets. Fig. 1b shows the XRD patterns of  $\text{SnS}_2/\text{CC}$  and Mo-SnS<sub>2</sub>/CC. Excluding the peaks of CC, both samples display a pure hexagonal  $\text{SnS}_2$  phase (JCPDS no. 23-677) with no detectable impurities. Obviously, all the peaks of Mo-SnS<sub>2</sub>/CC are much weaker than those of  $\text{SnS}_2/\text{CC}$ , indicating the lowered crystallinity of Mo-SnS<sub>2</sub> caused by Mo-doping. The morphologies of  $\text{SnS}_2$  and Mo-SnS<sub>2</sub> nanosheets were further investigated by scanning electron microscopy (SEM), transmission electron microscopy (TEM) and high-resolution TEM (HRTEM). The SEM images show that bushy nanosheets are densely and vertically anchored on the CC for both  $\text{SnS}_2/\text{CC}$  (Fig. 1c) and Mo-SnS<sub>2</sub>/CC (Fig. 1d). The nanosheet features can be further revealed by TEM with the observation of clear wrinkles and corrugations on  $\text{SnS}_2$  (Fig. 1e) and Mo-SnS<sub>2</sub> (Fig. 1f) nanosheets.<sup>39–41</sup> The HRTEM image shows that the pristine  $\text{SnS}_2$  nanosheets (Fig. 1g) possess a high crystallinity as evidenced by the sharp lattice fringes with a spacing value of 0.59 nm, assigned to the (001) facet of  $\text{SnS}_2$ . In contrast, blurred and discontinuous lattice fringes can be observed in Mo-SnS<sub>2</sub> nanosheets (Fig. 1h), indicating that Mo-doping can remarkably reduce the crystallinity of Mo-SnS<sub>2</sub> nanosheets, consistent with the XRD analysis (Fig. 1b). The selected areas in Fig. 1h (A and B squares), when applying an Inverse Fast Fourier Transform (IFFT) mask, display obvious distortions and dislocations in the lattice fringes,<sup>42–44</sup> suggesting the existence of plentiful defects (*i.e.*, vacancies) in Mo-SnS<sub>2</sub> nanosheets, which rationalizes the reduced crystallinity of Mo-SnS<sub>2</sub>. The scanning TEM (STEM) elemental mapping images (Fig. 1i) reveal that considerable Mo dopants are uniformly distributed on the entire surface of Mo-SnS<sub>2</sub> nanosheets.

The vacancies existing in Mo-SnS<sub>2</sub> nanosheets were further investigated by a combination of XPS, electron paramagnetic resonance (EPR) spectroscopy and DFT analysis. For both  $\text{SnS}_2$  and Mo-SnS<sub>2</sub> nanosheets, the XPS Sn3d spectra (Fig. 2a) reveal Sn3d<sub>5/2</sub> ( $\sim 486 \text{ eV}$ ) and Sn3d<sub>3/2</sub> ( $\sim 495 \text{ eV}$ ) states of  $\text{Sn}^{4+}$ , and the S2p spectra (Fig. 2b) reveal S2p<sub>3/2</sub> ( $\sim 161 \text{ eV}$ ) and S2p<sub>1/2</sub> ( $\sim 163 \text{ eV}$ ) states of  $\text{S}^{2-}$ . With respect to those of the pristine  $\text{SnS}_2$  nanosheets, the Sn3d and S2p spectra of Mo-SnS<sub>2</sub> nanosheets are negatively shifted by 0.4 and 0.3 eV, respectively, suggesting the decreased valence state and increased electrons in Mo-SnS<sub>2</sub> nanosheets caused by the presence of  $V_s$ .<sup>45</sup> The existence of enriched  $V_s$  in Mo-SnS<sub>2</sub> nanosheets can also be directly verified from the remarkably reduced atomic ratio of S/Mo from 1.88 ( $\text{SnS}_2$ ) to 1.62 (Mo-SnS<sub>2</sub>) derived from the XPS element analysis. In the EPR spectra (Fig. 2c), the signal at  $g = 2.001$  represents the electrons trapped in  $V_s$ . Compared to  $\text{SnS}_2$  nanosheets, Mo-SnS<sub>2</sub> nanosheets exhibit a much stronger EPR signal intensity, suggesting a higher concentration of  $V_s$ ,<sup>23</sup> consistent with the XPS results. To gain further insight, DFT was applied to predict the  $V_s$  formation energy ( $E_f$ ). As shown in Fig. 2d, the formation of isolated  $V_s$  in  $\text{SnS}_2$  requires a largely positive  $E_f$  (5.25 eV) and thus is thermodynamically unfavorable. With the introduction of the Mo dopant (Fig. 2e),  $V_s$  can be favorably formed at the Mo-adjacent site of Mo-SnS<sub>2</sub>- $V_s$  with a significantly reduced  $E_f$  ( $-0.78 \text{ eV}$ ). Therefore, the DFT results concur well with the XPS/EPR measurements and demonstrate that Mo-doping can considerably lower the  $V_s$  formation energy and enable the spontaneous generation of  $V_s$  in Mo-SnS<sub>2</sub> nanosheets.

DFT calculations were used to further investigate the electronic structure of Mo-SnS<sub>2</sub>- $V_s$ . From the electron contour maps sliced along the (001) plane, it can be seen that more electrons are accumulated in the Mo/ $V_s$  region in Mo-SnS<sub>2</sub>- $V_s$  (Fig. 2g) as compared to  $\text{SnS}_2$  (Fig. 2f), which is also confirmed by the differential charge density (Fig. S1†). Upon  $\text{N}_2$  adsorption, it is believed that these Mo/ $V_s$ -induced abundant accumulated electrons can be easily transferred into the anti-bonding orbitals of  $\text{N}_2$  molecules for the weakening and dissociation of the  $\text{N}\equiv\text{N}$  bond.<sup>46</sup> Projected density of states (PDOS, Fig. 2h) analysis indicates that  $\text{SnS}_2$  possesses a 0.64 eV bandgap indicative of its semiconducting character. In contrast, the co-presence of the Mo-dopant and  $V_s$  creates noticeable electronic states crossing the Fermi level, leading to the metallic characteristics of Mo-SnS<sub>2</sub>- $V_s$  and thus higher conductivity relative to that of  $\text{SnS}_2$ , which is favorable for the proton-coupled electron-transfer process to boost the NRR kinetics. Meanwhile, the calculated work function (Fig. 2i & S2†) indicates that Mo-SnS<sub>2</sub>- $V_s$  (5.513 eV) possesses a lower work function than  $\text{SnS}_2$  (6.758 eV), which suggests the higher capability of Mo-SnS<sub>2</sub>- $V_s$  for electron back-donation from its active sites to the absorbed  $\text{N}_2$  and NRR intermediates,<sup>47–49</sup> thus facilitating  $\text{N}_2$  adsorption, activation, and hydrogenation.

The electrocatalytic NRR performance of Mo-SnS<sub>2</sub>/CC as a self-standing electrode was examined in  $\text{N}_2$ -saturated 0.5 M  $\text{LiClO}_4$  using a gas-tight two-compartment cell, as displayed in Fig. S3.† An absorber was placed at the end of the cell to prevent the loss of produced  $\text{NH}_3$  by  $\text{N}_2$  flow during the NRR test.<sup>50</sup> All potentials were converted into values *versus* the reversible

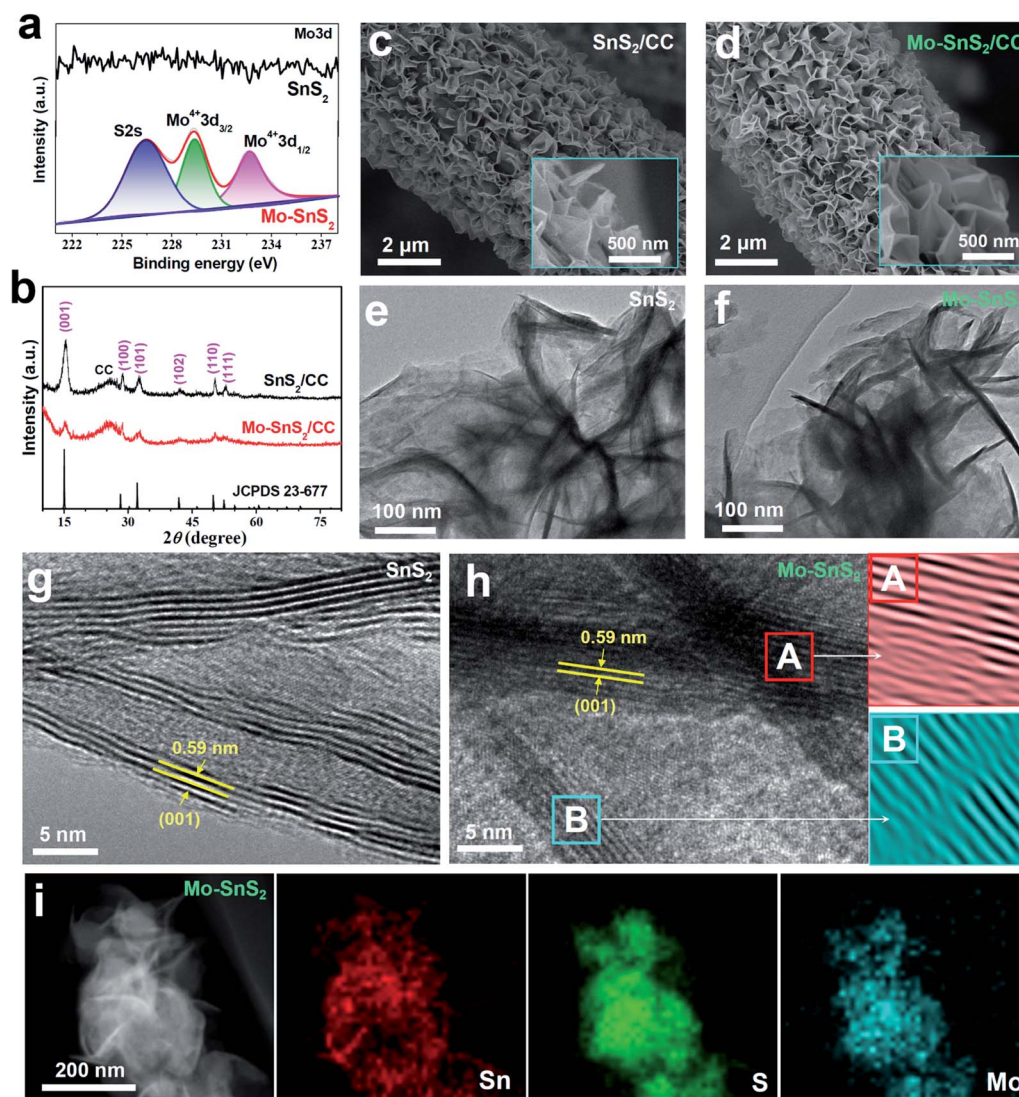


**Fig. 1** (a) XPS Mo3d spectrum of SnS<sub>2</sub> and Mo-SnS<sub>2</sub> nanosheets scraped from CC. (b) XRD patterns for SnS<sub>2</sub>/CC and Mo-SnS<sub>2</sub>/CC. (c and d) SEM images of (c) SnS<sub>2</sub>/CC and (d) Mo-SnS<sub>2</sub>/CC. (e and f) TEM images of (e) SnS<sub>2</sub> and (f) Mo-SnS<sub>2</sub> nanosheets. (g and h) HRTEM images of (g) SnS<sub>2</sub> and (h) Mo-SnS<sub>2</sub> nanosheets (A and B are the corresponding IFFT images recorded from regions A and B in (h)). (i) STEM element mapping images for Mo-SnS<sub>2</sub> nanosheets.

hydrogen electrode (*vs.* RHE), and the standard RHE was experimentally calibrated using cyclic voltammetry curves in a high-purity hydrogen saturated solution (Fig. S4†).<sup>36</sup> The concentration of generated NH<sub>3</sub> was experimentally determined by the indophenol blue method,<sup>51</sup> while the concentration of the possible N<sub>2</sub>H<sub>4</sub> as a byproduct was measured by the Watt-Chrisp approach.<sup>52</sup> Their standard calibration curves are shown in Fig. S5 and S6.† As displayed in Fig. S7,† N<sub>2</sub>H<sub>4</sub> can hardly be detected, implying a high NRR selectivity for Mo-SnS<sub>2</sub>/CC for N<sub>2</sub>-to-NH<sub>3</sub> conversion.

The polarization curves recorded by linear sweep voltammetry (LSV, Fig. 3a) show a higher current density in N<sub>2</sub>-saturated solution than in Ar-saturated solution, suggesting the feasibility of the NRR on Mo-SnS<sub>2</sub>/CC. Before the quantitative evaluation of the NRR performance, a series of control tests were preliminarily carried out to exclude the possible influences

from any nitrogen contaminants.<sup>53</sup> The isotopic labeling measurements based on <sup>1</sup>H nuclear magnetic resonance (NMR) were first utilized to trace the origin of the N source, as shown in Fig. 3b. After NRR electrolysis using <sup>14</sup>N<sub>2</sub> or <sup>15</sup>N<sub>2</sub> as the feed gas, a triplet for <sup>14</sup>NH<sub>4</sub><sup>+</sup> (<sup>1</sup>J<sub>N-H</sub> = 52 Hz) or a doublet for <sup>15</sup>NH<sub>4</sub><sup>+</sup> (<sup>1</sup>J<sub>N-H</sub> = 72 Hz) can be distinguished, respectively, whereas no labeled <sup>14</sup>NH<sub>4</sub><sup>+</sup> or <sup>15</sup>NH<sub>4</sub><sup>+</sup> can be found when using Ar as the feed gas. In addition, UV-vis analysis (Fig. S8†) in an Ar-saturated solution, or at open circuit, or on pristine CC does not produce a detectable amount of NH<sub>3</sub>.<sup>54–56</sup> Furthermore, the time-dependent test (Fig. S9†) shows that the produced NH<sub>3</sub> increases linearly with the electrolysis time, indicating that NH<sub>3</sub> can be continuously generated by NRR catalysis over Mo-SnS<sub>2</sub>/CC. We also employed the ion chromatography (IC) technique to quantitatively determine the concentration of NRR-derived NH<sub>3</sub>. As depicted in Fig. 3c and S10,† the IC measurement (1.27 μg mL<sup>-1</sup>) is very



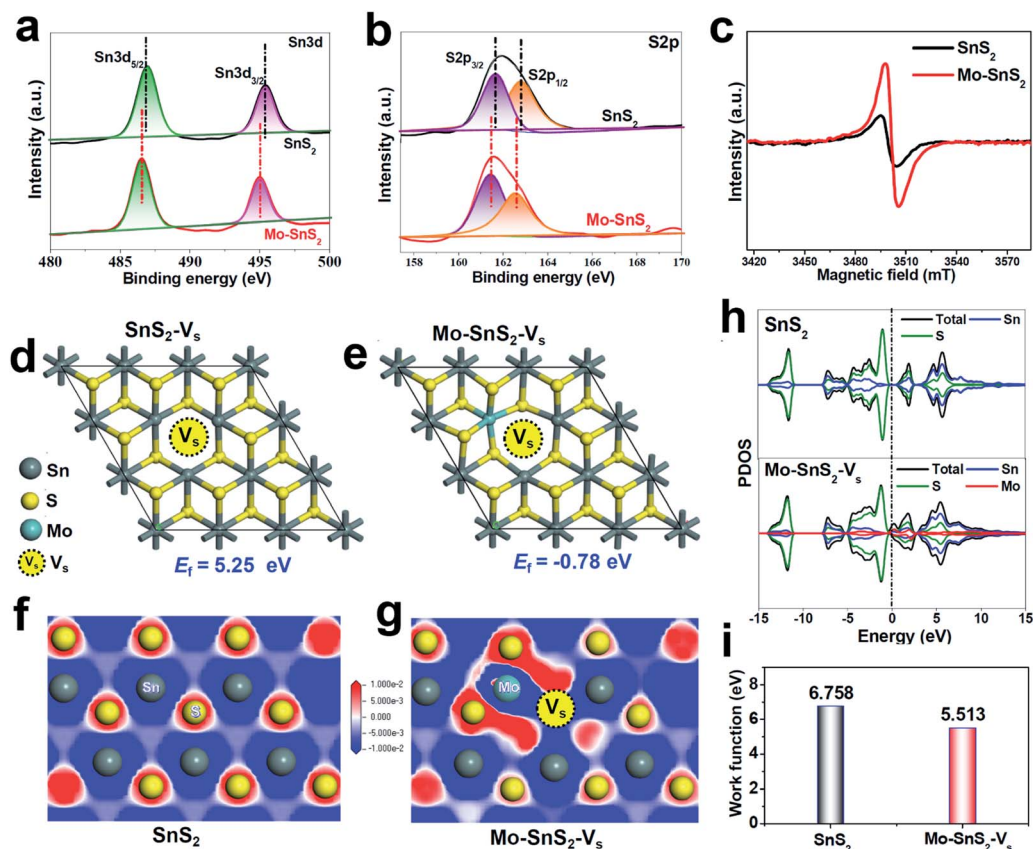


Fig. 2 (a and b) XPS spectra of  $\text{SnS}_2$  and  $\text{Mo-SnS}_2$  nanosheets: (a)  $\text{Sn}3d$  and (b)  $\text{S}2p$ . (c) EPR spectra of  $\text{SnS}_2$  and  $\text{Mo-SnS}_2$  nanosheets. (d and e) Optimized  $\text{SnS}_2$  structures with isolated  $\text{V}_s$  ( $\text{SnS}_2\text{-V}_s$ ) and Mo-adjacent  $\text{V}_s$  ( $\text{Mo-SnS}_2\text{-V}_s$ ), and the corresponding formation energies ( $E_f$ ). (f and g) Electron contour maps of the (001) slice for (f)  $\text{SnS}_2$  and (g)  $\text{Mo-SnS}_2\text{-V}_s$ . The blue and red regions represent electron depletion and accumulation, respectively. (h) PDOS of  $\text{SnS}_2$  and  $\text{Mo-SnS}_2\text{-V}_s$ . (i) Calculated work functions of  $\text{SnS}_2$  and  $\text{Mo-SnS}_2\text{-V}_s$  (Fig. S2†).

close to the  $1.15 \mu\text{g mL}^{-1}$  attained by the indophenol blue method with a reasonable margin of experimental error. Therefore, all these control experiments convincingly demonstrate that the produced  $\text{NH}_3$  originates from the NRR.

The NRR performance of  $\text{Mo-SnS}_2/\text{CC}$  was then quantitatively examined by the combination of chronoamperometry testing with each cycle for 2 h of electrolysis (Fig. 3d) and UV-vis analysis (average of three measurements) at various potentials. The corresponding data of  $\text{NH}_3$  yield and FE are shown in Fig. 3e. As observed, the NRR activity of  $\text{Mo-SnS}_2/\text{CC}$  exhibits optimum NRR performance with an  $\text{NH}_3$  yield of  $41.3 \mu\text{g h}^{-1} \text{mg}^{-1}$  at  $-0.5 \text{ V}$  and a faradaic efficiency of 20.8% at  $-0.4 \text{ V}$ . As shown in Table S1,†  $\text{Mo-SnS}_2/\text{CC}$  is the best  $\text{SnS}_2$ -based NRR catalyst reported to date and compares favorably to most state-of-the-art NRR catalysts. Nonetheless, the NRR performance shows a sharp decline at more negative potentials, which is attributed to the significantly enhanced HER.<sup>57</sup>

We also assessed the NRR performance of undoped  $\text{SnS}_2/\text{CC}$  for comparison under identical conditions. As shown in Fig. 3f,  $\text{SnS}_2/\text{CC}$  possesses a more inferior NRR activity with the highest  $\text{NH}_3$  yield of  $10.6 \mu\text{g h}^{-1} \text{mg}^{-1}$  at  $-0.5 \text{ V}$ , which is about one-quarter that of  $\text{Mo-SnS}_2/\text{CC}$  ( $41.3 \mu\text{g h}^{-1} \text{mg}^{-1}$ ), demonstrating that Mo-doping is able to dramatically promote the NRR activity of  $\text{SnS}_2$  nanosheets. To elucidate the NRR

enhancement observed in  $\text{Mo-SnS}_2/\text{CC}$ , we determined the electrochemically active surface area (ECSA) by measuring the double-layer capacitance ( $C_{dl}$ ). As shown in Fig. S11,†  $\text{Mo-SnS}_2/\text{CC}$  exhibits only a 1.3 times higher  $C_{dl}$ , but a  $\sim 3.9$  times higher  $\text{NH}_3$  yield than  $\text{SnS}_2/\text{CC}$ , suggesting that the ECSA is not the primary factor and  $\text{Mo-SnS}_2/\text{CC}$  is intrinsically more active than  $\text{SnS}_2/\text{CC}$ . In addition, as depicted in the electrochemical impedance spectra (EIS, Fig. S12†),  $\text{Mo-SnS}_2/\text{CC}$  delivers a smaller charge-transport resistance than  $\text{SnS}_2/\text{CC}$ , indicating faster electron-transfer and enhanced NRR reaction kinetics of  $\text{Mo-SnS}_2/\text{CC}$ . This can be attributed to the synergistic role of the Mo-dopant and  $\text{V}_s$  in improving the conductivity of  $\text{Mo-SnS}_2$ , as revealed by the DFT results (Fig. 2h). Therefore, the combined Mo-dopant and  $\text{V}_s$  can bring about an improved conductivity and elevated intrinsic NRR activity, resulting in significantly enhanced NRR performance of  $\text{Mo-SnS}_2/\text{CC}$ .

We further evaluate the NRR stability which is another critical factor for practical applications.<sup>58,59</sup> Chronopotentiometric response measurements (Fig. 3g) reveal that the current density over  $\text{Mo-SnS}_2/\text{CC}$  presents a negligible degeneration for at least 20 h of continuous electrolysis, verifying the excellent long-term stability. Besides, when conducting seven chronoamperometric runs for  $\text{Mo-SnS}_2/\text{CC}$ , there is no remarkable change in the UV-vis spectra of the resultant electrolytes (Fig. S13†), nor in the

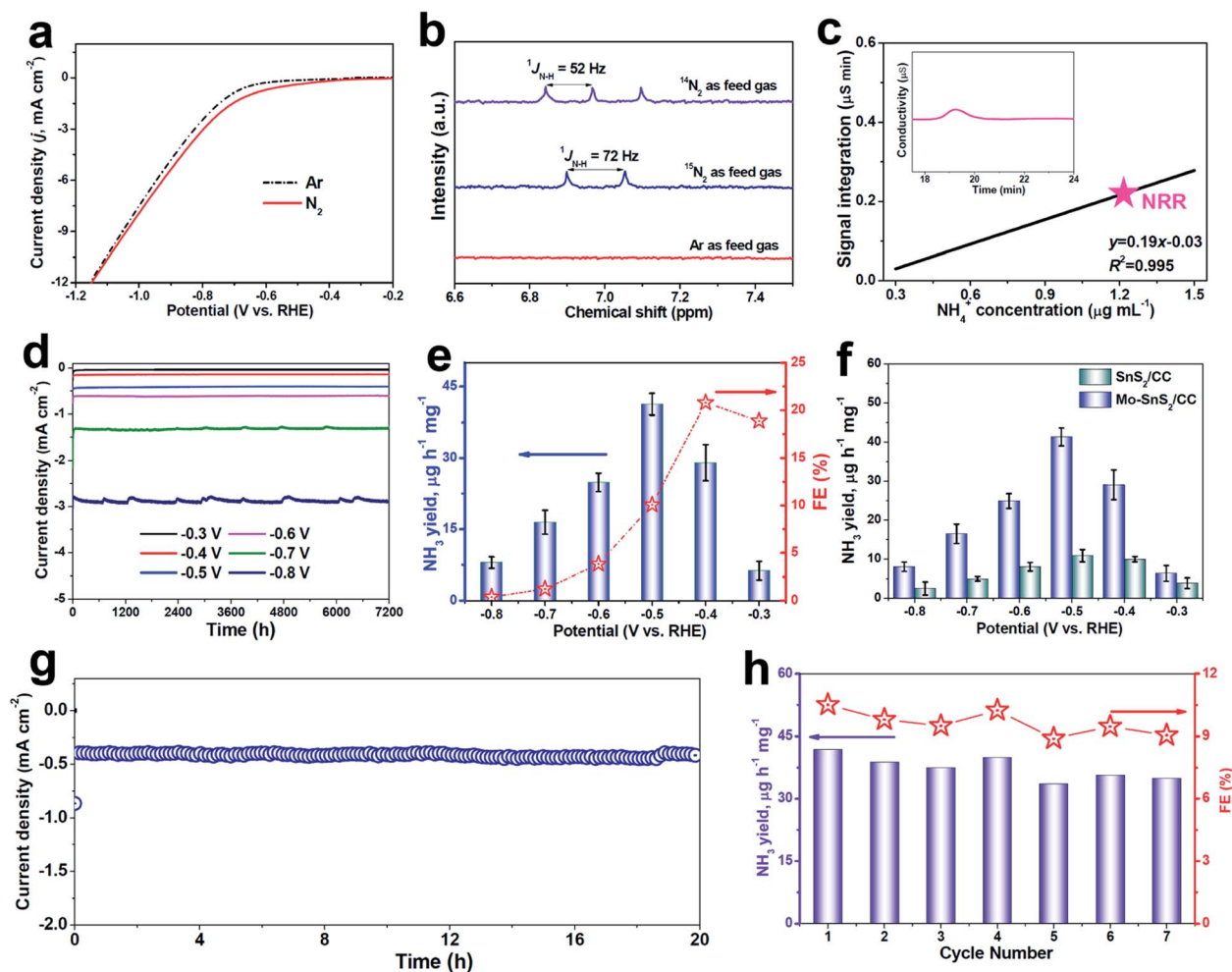


**Fig. 3** (a) LSV curves of Mo-SnS<sub>2</sub>/CC in Ar- and N<sub>2</sub>-saturated solutions. (b) <sup>1</sup>H NMR spectra of electrolytes after NRR electrolysis for 2 h on Mo-SnS<sub>2</sub>/CC using <sup>14</sup>N<sub>2</sub>, <sup>15</sup>N<sub>2</sub> or Ar as feed gases. (c) IC spectra of the electrolyte after NRR electrolysis on Mo-SnS<sub>2</sub>/CC for 2 h at −0.5 V (inset), and the determined NH<sub>4</sub><sup>+</sup> concentration of the electrolyte by referring to the calibration curve (Fig. S10†). (d) Chronoamperometry test results of Mo-SnS<sub>2</sub>/CC for 2 h of NRR electrolysis at various potentials, and (e) the corresponding NH<sub>3</sub> yields and FEs. (f) NH<sub>3</sub> yields of SnS<sub>2</sub>/CC and Mo-SnS<sub>2</sub>/CC at various potentials. (g) Chronoamperometry test results of Mo-SnS<sub>2</sub>/CC for 20 h of NRR electrolysis. (h) NH<sub>3</sub> yields and FEs of Mo-SnS<sub>2</sub>/CC for seven cycles (each for 2 h of electrolysis at −0.5 V).

resulting NH<sub>3</sub> yield and FE data (Fig. 3h), confirming the good cycling stability. Further, the morphology, crystal phase and chemical bonding states of Mo-SnS<sub>2</sub> nanosheets can be well preserved after the stability test, as evidenced by SEM/TEM (Fig. S14†), XRD (Fig. S15†) and XPS (Fig. S16†) measurements. The outstanding stability of Mo-SnS<sub>2</sub>/CC is believed to originate from the strong atomic and electronic bonding of Mo-dopants, 2D confinement effect of the nanosheet structure,<sup>29</sup> and direct nanosheet growth on CC with tight catalyst attachment.<sup>31</sup> Therefore, Mo-SnS<sub>2</sub>/CC has great potential as a promising catalyst for electroreduction of N<sub>2</sub> to NH<sub>3</sub> with a favorable NH<sub>3</sub> production rate and robust stability.

DFT calculations based on the energetically stable Mo-SnS<sub>2</sub>-V<sub>s</sub> structure (Fig. 2e) were further performed to gain deep insights into the synergistic role of the Mo-dopant and V<sub>s</sub> in facilitating the NRR. In view of N<sub>2</sub> adsorption as the critical step to initialize the NRR, N<sub>2</sub> adsorption behaviors over pristine SnS<sub>2</sub> and Mo-SnS<sub>2</sub>-V<sub>s</sub> were first analyzed. For pristine SnS<sub>2</sub> (Fig. 4a

and b), the N<sub>2</sub> molecule barely adsorbs on either the central Sn site (Fig. 4a) or the edge Sn site (Fig. 4b), as evidenced by the negligible charge transfer and much less N≡N bond elongation (1.105 Å for the original N<sub>2</sub> gas), suggesting that pristine SnS<sub>2</sub> is almost inactive for the NRR. In sharp contrast, after N<sub>2</sub> adsorption on the V<sub>s</sub> site of Mo-SnS<sub>2</sub>-V<sub>s</sub> (Fig. 4c), the N≡N bond is considerably elongated to 1.211 Å and 0.55|e| is injected into \*N<sub>2</sub>, implying the greatly enhanced N<sub>2</sub> adsorption on Mo-SnS<sub>2</sub>-V<sub>s</sub>. The enlarged view (Fig. 4d) reveals a unique N<sub>2</sub> adsorption mode on the V<sub>s</sub> site of Mo-SnS<sub>2</sub>-V<sub>s</sub>, that is, the N<sub>2</sub> molecule is fixed to the Mo-Sn-Sn trimer center *via* a side-on configuration. Meanwhile, the N≡N triple bond is even cleaved to the N=N double bond without hydrogenation, indicating that the Mo-Sn-Sn trimer can strongly activate N<sub>2</sub> through an analogous dissociative pattern. As shown in the PDOS of the Mo-Sn-Sn trimer after N<sub>2</sub> adsorption (Fig. 4e), the Mo4d and Sn5p orbitals are both considerably hybridized with the N2p orbitals both below and above the Fermi level, suggesting the efficient back-

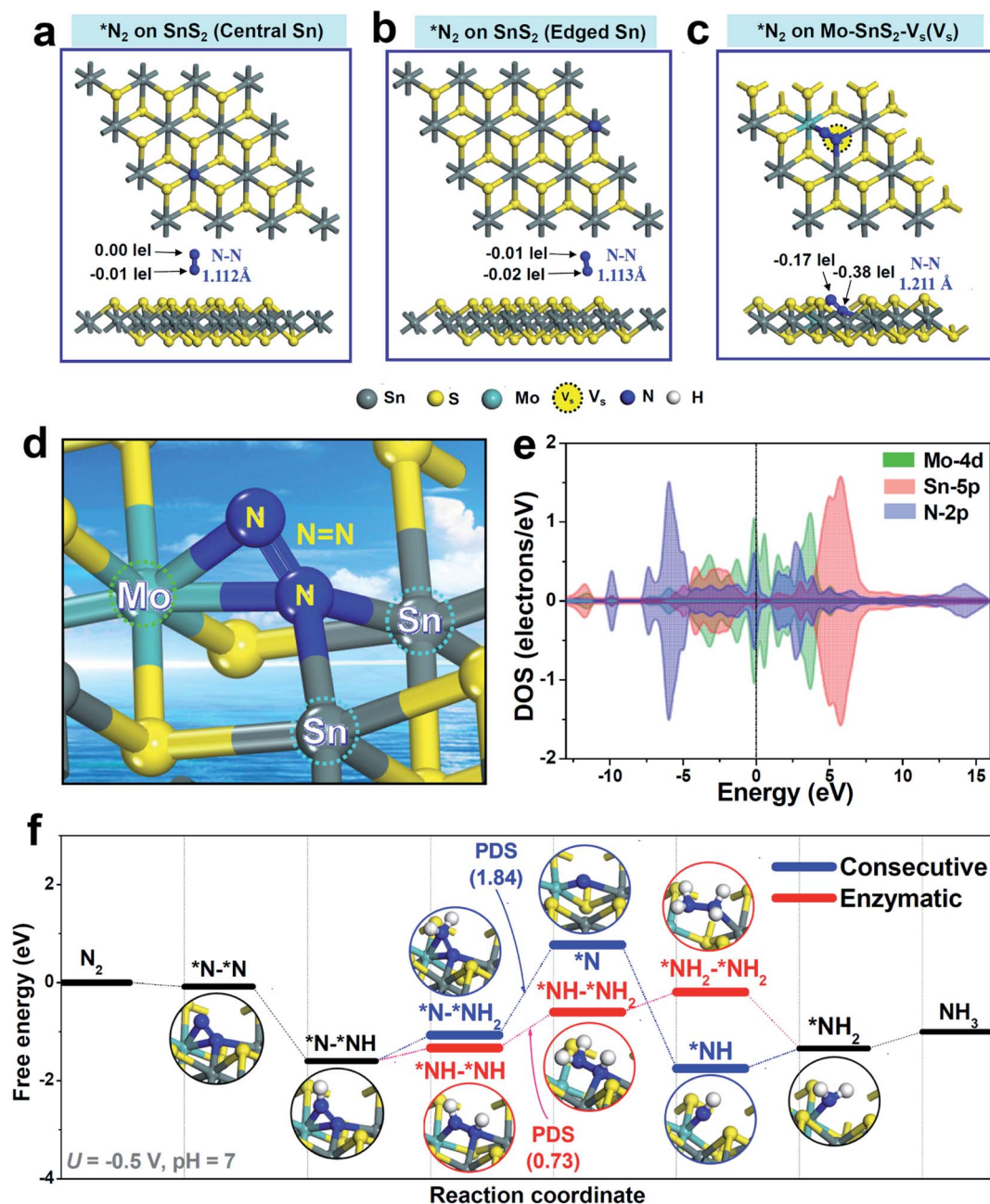


Fig. 4 (a–c) Optimized structures of  $\text{N}_2$  adsorption on (a)  $\text{SnS}_2$  (central Sn site), (b)  $\text{SnS}_2$  (edge Sn site) and (c)  $\text{Mo-SnS}_2\text{-V}_s$  ( $\text{V}_s$  site). (d) Enlarged view of the  $\text{N}_2$  adsorption mode on a  $\text{V}_s$  site of  $\text{Mo-SnS}_2\text{-V}_s$  (Mo–Sn–Sn trimer). (e) PDOS of the Mo–Sn–Sn trimer after  $\text{N}_2$  adsorption. (f) Free energy diagrams of NRR consecutive/enzymatic reaction pathways over the Mo–Sn–Sn trimer at  $U = -0.5$  V, pH = 7.

donation of electrons from the Mo–Sn–Sn trimer to  $\text{N}_2$ .<sup>60,61</sup> The prominent back-donation of electrons from the Mo–Sn–Sn trimer to  $\text{N}_2$  can be directly visualized from the differential charge density (Fig. S17†), showing the pronouncedly accumulated electrons on  $\text{N}_2$ . Mulliken charge analysis (Fig. S18†) reveals that the Mo–Sn–Sn trimer back-donates a total of  $0.55|e|$  to  $\text{N}_2$ , with  $0.37|e|$  from the Mo dopant and  $0.09|e|$  from each of the two Sn atoms. Hence, the co-presence of the Mo dopant and  $\text{V}_s$  in  $\text{Mo-SnS}_2\text{-V}_s$  enables the creation of Mo–Sn–Sn trimer catalytic sites that can strongly activate the  $\text{N}_2$  molecule even for the cleavage of the  $\text{N}\equiv\text{N}$  triple bond to the  $\text{N}=\text{N}$  double bond at the  $\text{N}_2$  adsorption stage.

The hydrogenation pathway of  $\text{Mo-SnS}_2\text{-V}_s$  was then evaluated using Gibbs free energy profiles through the consecutive (analogous to the distal pathway but *via* side-on configuration<sup>62</sup>) and enzymatic associative mechanisms, as shown in Fig. 4f. Optimized structures of all the NRR intermediates are presented in Fig. S19† (consecutive) and Fig. S20† (enzymatic). Notably, with the strong  $\text{N}_2$  activation by the Mo–Sn–Sn trimer, the free energy of  $\text{N}_2 \rightarrow \text{N}^*-\text{NH}$  even becomes negative, making the first hydrogenation step ( $\text{N}_2 \rightarrow \text{N}^*-\text{NH}$ ) occur spontaneously. This is in stark contrast to the largely positive free energy of  $\text{N}^*-\text{NH}$  (2.19 eV) observed in pristine  $\text{SnS}_2$ ,<sup>22</sup> which has the first hydrogenation step ( $\text{N}_2 \rightarrow \text{N}^*-\text{NH}$ ) as the potential



determining step (PDS). After the first hydrogenation,  $*N-*NH$  can be further hydrogenated through a consecutive or enzymatic pathway. For the consecutive pathway,  $*N-*NH_2 \rightarrow *N$  is the PDS with a high energy barrier of 1.84 eV, while the PDS energy barrier ( $*NH-*NH \rightarrow *NH-*NH_2$ ) is substantially reduced to 0.73 eV for the enzymatic pathway. Hence, the hydrogenation of  $Mo-SnS_2-V_s$  prefers to proceed *via* the enzymatic pathway with an overpotential of 0.57 V,<sup>63</sup> which is theoretically lower than that of most reported NRR catalysts.<sup>64–67</sup> These results demonstrate that the highly active  $Mo-Sn-Sn$  trimer provides  $Mo-SnS_2-V_s$  with the downhill process of the first hydrogenation step, leading to the significantly decreased energy barrier and largely enhanced NRR activity.

On the other hand, as reported in the literature,<sup>68,69</sup> the surface charge and hydrogen bonding can affect the electrocatalytic calculations. As shown in Fig. S21,† after considering the effects of surface charge (adding one charge  $e^-$  in the catalyst system) and hydrogen bonding (adding two  $H_2O$  molecules on the catalyst surface), we find that these two factors can make the free energies of  $*N_2$  and  $*N-*NH$  become more negative but the downhill trend of the  $*N_2 \rightarrow *N-*NH$  process still remains. Therefore, our main conclusion is not affected by the effects of surface charge and hydrogen bonding.

In conclusion, through combined experimental and theoretical investigations, we demonstrated that the synergistic modulation of vacancy engineering and heteroatom doping has been successfully achieved in  $Mo-SnS_2$  nanosheets with enriched  $V_s$ , which showed greatly enhanced NRR performance with an  $NH_3$  yield of  $41.3 \mu g h^{-1} mg^{-1}$  (−0.5 V) and an FE of 20.8% (−0.4 V). DFT calculations revealed the unique NRR mechanism of  $Mo-SnS_2-V_s$ , in which the created  $Mo-Sn-Sn$  trimer active sites could strongly activate  $N_2$  for even the cleavage of the  $N \equiv N$  triple bond to the  $N = N$  double bond at the  $N_2$  adsorption stage, consequently resulting in a downhill process of the first hydrogenation step and a largely reduced energy barrier. This work not only offers an efficient strategy towards the design of  $SnS_2$ -based catalysts for highly efficient electrosynthesis of  $NH_3$ , but also provides new insights into the synergistic role of vacancies and dopants in regulating the NRR activity.

## Conflicts of interest

There are no conflicts of interest to declare.

## Acknowledgements

This work is supported by the National Natural Science Foundation of China (51761024), “Feitian Scholar” Program of Gansu Province, CAS “Light of West China” Program, and Foundation of A Hundred Youth Talents Training Program of Lanzhou Jiaotong University.

## References

- 1 J. A. Brandes, N. Z. Boctor, G. D. Cody, B. A. Cooper, R. M. Hazen and H. S. Yoder Jr, *Nature*, 1998, **395**, 365.

- 2 X. Zhu, S. Mou, Q. Peng, Q. Liu, Y. Luo, G. Chen, S. Gao and X. Sun, *J. Mater. Chem. A*, 2020, **8**, 1545–1556.
- 3 G. F. Chen, S. Y. Ren, L. L. Zhang, H. Cheng, Y. R. Luo, K. H. Zhu, L. X. Ding and H. H. Wang, *Small Methods*, 2019, **3**, 1800337.
- 4 S. J. Li, D. Bao, M. M. Shi, B. R. Wulan, J. M. Yan and Q. Jiang, *Adv. Mater.*, 2017, **29**, 1700001.
- 5 H. Xie, Q. Geng, X. Zhu, Y. Luo, L. Chang, X. Niu, X. Shi, A. M. Asiri, S. Gao, Z. Wang and X. Sun, *J. Mater. Chem. A*, 2019, **7**, 24760–24764.
- 6 R. Zhao, C. Liu, X. Zhang, X. Zhu, P. Wei, L. Ji, Y. Guo, S. Gao, Y. Luo, Z. Wang and X. Sun, *J. Mater. Chem. A*, 2020, **8**, 77–81.
- 7 G. Deng, T. Wang, A. A. Alshehri, K. A. Alzahrani, Y. Wang, H. Ye, Y. Luo and X. Sun, *J. Mater. Chem. A*, 2019, **7**, 21674–21677.
- 8 H. Xian, Q. Wang, G. Yu, H. Wang, Y. Li, Y. Wang and T. Li, *Appl. Catal., A*, 2019, **581**, 116–122.
- 9 G. Yu, H. Guo, S. Liu, L. Chen, A. A. Alshehri, K. A. Alzahrani, F. Hao and T. Li, *ACS Appl. Mater. Interfaces*, 2019, **11**, 35764–35769.
- 10 H. Xian, H. Guo, Z. Chen, G. Yu, A. A. Alshehri, K. A. Alzahrani, F. Hao, R. Song and T. Li, *ACS Appl. Mater. Interfaces*, 2020, **12**, 2445–2451.
- 11 Y. R. Luo, G. F. Chen, L. Ding, X. Z. Chen, L. X. Ding and H. H. Wang, *Joule*, 2019, **3**, 279–289.
- 12 H. Cheng, L. X. Ding, G. F. Chen, L. L. Zhang, J. Xue and H. H. Wang, *Adv. Mater.*, 2018, **30**, 1803694.
- 13 K. Chu, Q. Q. Li, Y. H. Cheng and Y. P. Liu, *ACS Appl. Mater. Interfaces*, 2020, **12**, 11789–11796.
- 14 H. Cheng, P. X. Cui, F. R. Wang, L. X. Ding and H. H. Wang, *Angew. Chem., Int. Ed.*, 2019, **58**, 15541–15547.
- 15 X. Zhu, T. Wu, L. Ji, C. Li, T. Wang, S. Wen, S. Gao, X. Shi, Y. Luo, Q. Peng and X. Sun, *J. Mater. Chem. A*, 2019, **7**, 16117–16121.
- 16 L. Xia, X. Wu, Y. Wang, Z. Niu, Q. Liu, T. Li, X. Shi, A. M. Asiri and X. Sun, *Small Methods*, 2018, **3**, 1800251.
- 17 K. Chu, Q. Li, Y. Liu, J. Wang and Y. Cheng, *Appl. Catal., B*, 2020, **267**, 118693.
- 18 L. L. Zhang, L. X. Ding, G. F. Chen, X. F. Yang and H. H. Wang, *Angew. Chem., Int. Ed.*, 2019, **131**, 2638–2642.
- 19 L. Xia, J. Yang, H. Wang, R. Zhao, H. Chen, W. Fang, A. M. Asiri, F. Xie, G. Cui and X. Sun, *Chem. Commun.*, 2019, **55**, 3371–3374.
- 20 F. Li, L. Chen, G. P. Knowles, D. R. MacFarlane and J. Zhang, *Angew. Chem., Int. Ed.*, 2017, **56**, 505–509.
- 21 P. Li, W. Fu, P. Zhuang, Y. Cao, C. Tang, A. B. Watson, P. Dong, J. Shen and M. Ye, *Small*, 2019, **15**, 1902535.
- 22 X. Chen, Y.-T. Liu, C. Ma, J. Yu and B. Ding, *J. Mater. Chem. A*, 2019, **7**, 22235–22241.
- 23 Y. B. Li, Y. P. Liu, J. Wang, Y. L. Guo and K. Chu, *Inorg. Chem. Front.*, 2020, **7**, 455–463.
- 24 L. Yang, T. Wu, R. Zhang, H. Zhou, L. Xia, X. Shi, H. Zheng, Y. Zhang and X. Sun, *Nanoscale*, 2019, **11**, 1555–1562.
- 25 Z. Sun, R. Huo, C. Choi, S. Hong, T.-S. Wu, J. Qiu, C. Yan, Z. Han, Y. Liu, Y.-L. Soo and Y. Jung, *Nano Energy*, 2019, **62**, 869–875.

- 26 L. Zhang, X.-Y. Xie, H. Wang, L. Ji, Y. Zhang, H. Chen, T. Li, Y. Luo, G. Cui and X. Sun, *Chem. Commun.*, 2019, **55**, 4627–4630.
- 27 C. Lv, Y. Qian, C. Yan, Y. Ding, Y. Liu, G. Chen and G. Yu, *Angew. Chem., Int. Ed.*, 2018, **57**, 10246–10250.
- 28 X. Yang, J. Nash, J. Anibal, M. Dunwell, S. Kattel, E. Stavitski, K. Attenkofer, J. G. Chen, Y. Yan and B. Xu, *J. Am. Chem. Soc.*, 2018, **140**, 13387–13391.
- 29 H. Jin, L. Li, X. Liu, C. Tang, W. Xu, S. Chen, L. Song, Y. Zheng and S.-Z. Qiao, *Adv. Mater.*, 2019, **31**, 1902709.
- 30 X. H. Wang, J. Wang, Y. B. Li and K. Chu, *ChemCatChem*, 2019, **11**, 4529–4536.
- 31 Y. P. Liu, Y. B. Li, H. Zhang and K. Chu, *Inorg. Chem.*, 2019, **58**, 10424–10431.
- 32 K. Chu, Y. Liu, Y. Chen and Q. Li, *J. Mater. Chem. A*, 2020, **8**, 5200–5208.
- 33 K. Chu, Y. H. Chen, Q. Q. Li, Y. P. Liu and Y. Tian, *J. Mater. Chem. A*, 2020, **8**, 5865–5873.
- 34 T. Wu, W. Kong, Y. Zhang, Z. Xing, J. Zhao, T. Wang, X. Shi, Y. Luo and X. Sun, *Small Methods*, 2019, 1900356.
- 35 C. Guo, X. Liu, L. Gao, X. Kuang, X. Ren, X. Ma, M. Zhao, H. Yang, X. Sun and Q. Wei, *Appl. Catal., B*, 2020, **263**, 118296.
- 36 K. Chu, Y. P. Liu, Y. B. Li, Y. L. Guo, Y. Tian and H. Zhang, *Appl. Catal., B*, 2020, **264**, 118525.
- 37 T. Wu, Z. Xing, S. Mou, C. Li, Y. Qiao, Q. Liu, X. Zhu, Y. Luo, X. Shi, Y. Zhang and X. Sun, *Angew. Chem., Int. Ed.*, 2019, **58**, 18449–18453.
- 38 N. Cao, Z. Chen, K. Zang, J. Xu, J. Zhong, J. Luo, X. Xu and G. Zheng, *Nat. Commun.*, 2019, **10**, 1–12.
- 39 K. Chu, X. H. Wang, Y. B. Li, D. J. Huang, Z. R. Geng, X. L. Zhao, H. Liu and H. Zhang, *Mater. Des.*, 2018, **140**, 85–94.
- 40 K. Chu, J. Wang, Y. P. Liu and Z. R. Geng, *Carbon*, 2018, **140**, 112–123.
- 41 K. Chu, X. H. Wang, F. Wang, Y. B. Li, D. J. Huang, H. Liu, W. L. Ma, F. X. Liu and H. Zhang, *Carbon*, 2018, **127**, 102–112.
- 42 K. Chu, J. Wang, Y. P. Liu, Y. B. Li, C. C. Jia and H. Zhang, *Carbon*, 2019, **143**, 85–96.
- 43 K. Chu, F. Wang, X. H. Wang, Y. B. Li, Z. R. Geng, D. J. Huang and H. Zhang, *Mater. Des.*, 2018, **144**, 290–303.
- 44 K. Chu, F. Wang, Y. B. Li, X. H. Wang, D. J. Huang and H. Zhang, *Carbon*, 2018, **133**, 127–139.
- 45 L. Meng, S. Wang, F. Cao, W. Tian, R. Long and L. Li, *Angew. Chem., Int. Ed.*, 2019, **58**, 6761–6765.
- 46 M.-A. Légaré, G. Bélanger-Chabot, R. D. Dewhurst, E. Welz, I. Krummenacher, B. Engels and H. Braunschweig, *Science*, 2018, **359**, 896–900.
- 47 J. Wang, Y. P. Liu, H. Zhang, D. J. Huang and K. Chu, *Catal. Sci. Technol.*, 2019, **9**, 4248–4254.
- 48 Y. P. Liu, Y. B. Li, D. J. Huang, H. Zhang and K. Chu, *Chem.–Eur. J.*, 2019, **25**, 11933–11939.
- 49 K. Chu, Y. P. Liu, Y. B. Li, J. Wang and H. Zhang, *ACS Appl. Mater. Interfaces*, 2019, **11**, 31806–31815.
- 50 L. Li, C. Tang, B. Xia, H. Jin, Y. Zheng and S.-Z. Qiao, *ACS Catal.*, 2019, **9**, 2902–2908.
- 51 D. Zhu, L. Zhang, R. E. Ruther and R. J. Hamers, *Nat. Mater.*, 2013, **12**, 836.
- 52 G. W. Watt and J. D. Chrisp, *Anal. Chem.*, 1952, **24**, 2006–2008.
- 53 K. Chu, Y. P. Liu, Y. B. Li, Y. L. Guo and Y. Tian, *ACS Appl. Mater. Interfaces*, 2020, **12**, 7081–7090.
- 54 J. Yu, C. Li, B. Li, X. Zhu, R. Zhang, L. Ji, D. Tang, A. M. Asiri, X. Sun, Q. Li, S. Liu and Y. Luo, *Chem. Commun.*, 2019, **55**, 6401–6404.
- 55 R. Zhang, L. Ji, W. Kong, H. Wang, R. Zhao, H. Chen, T. Li, B. Li, Y. Luo and X. Sun, *Chem. Commun.*, 2019, **55**, 5263–5266.
- 56 C. Li, J. Yu, L. Yang, J. Zhao, W. Kong, T. Wang, A. M. Asiri, Q. Li and X. Sun, *Inorg. Chem.*, 2019, **58**, 9597–9601.
- 57 A. R. Singh, B. A. Rohr, J. A. Schwalbe, M. Cargnello, K. Chan, T. F. Jaramillo, I. Chorkendorff and J. K. Nørskov, *ACS Catal.*, 2016, **7**, 706–709.
- 58 P. Wang, Q. Q. Li, Y. H. Cheng and K. Chu, *J. Mater. Sci.*, 2020, **55**, 4624–4632.
- 59 F. Wang, Y. P. Liu, H. Zhang and K. Chu, *ChemCatChem*, 2019, **11**, 1441–1447.
- 60 Q. Li, L. He, C. Sun and X. Zhang, *J. Phys. Chem. C*, 2017, **121**, 27563–27568.
- 61 Y.-C. Hao, Y. Guo, L.-W. Chen, M. Shu, X.-Y. Wang, T.-A. Bu, W.-Y. Gao, N. Zhang, X. Su, X. Feng, J.-W. Zhou, B. Wang, C.-W. Hu, A.-X. Yin, R. Si, Y.-W. Zhang and C.-H. Yan, *Nat. Catal.*, 2019, **2**, 448–456.
- 62 L. Shi, Q. Li, C. Ling, Y. Zhang, Y. Ouyang, X. Bai and J. Wang, *J. Mater. Chem. A*, 2019, **7**, 4865–4871.
- 63 J. Zhao and Z. Chen, *J. Am. Chem. Soc.*, 2017, **139**, 12480–12487.
- 64 K. Chu, Y. Liu, J. Wang and H. Zhang, *ACS Appl. Energy Mater.*, 2019, **2**, 2288–2295.
- 65 K. Chu, Y. Liu, Y. Li, H. Zhang and Y. Tian, *J. Mater. Chem. A*, 2019, **7**, 4389–4394.
- 66 Z. Wang, F. Gong, L. Zhang, R. Wang, L. Ji, Q. Liu, Y. Luo, H. Guo, Y. Li, P. Gao, X. Shi, B. Li, B. Tang and X. Sun, *Adv. Sci.*, 2018, 1801182.
- 67 X. Li, T. Li, Y. Ma, Q. Wei, W. Qiu, H. Guo, X. Shi, P. Zhang, A. M. Asiri, L. Chen, B. Tang and X. Sun, *Adv. Energy Mater.*, 2018, **8**, 1801357.
- 68 X. Zhao and Y. Liu, *J. Am. Chem. Soc.*, 2020, **142**, 5773–5777.
- 69 D. Kim, J. Shi and Y. Liu, *J. Am. Chem. Soc.*, 2018, **140**, 9127–9131.